Nanoscale

PAPER

View Article Online
View Journal | View Issue

Cite this: *Nanoscale*, 2016, **8**, 12013

Effects of *para*-substituents of styrene derivatives on their chemical reactivity on platinum nanoparticle surfaces†

Peiguang Hu, Limei Chen, Christopher P. Deming, Jia-En Lu, Lewis W. Bonny and Shaowei Chen*

Received 19th March 2016,
Accepted 19th May 2016

DOI: 10.1039/c6nr02296k

www.rsc.org/nanoscale

Stable platinum nanoparticles were successfully prepared by the self-assembly of *para*-substituted styrene derivatives onto the platinum surfaces as a result of platinum-catalyzed dehydrogenation and transformation of the vinyl groups to the acetylene ones, forming platinum–vinylidene/–acetylide interfacial bonds. Transmission electron microscopic measurements showed that the nanoparticles were well dispersed without apparent aggregation, suggesting sufficient protection of the nanoparticles by the organic capping ligands, and the average core diameter was estimated to be 2.0 ± 0.3 nm, 1.3 ± 0.2 nm, and 1.1 ± 0.2 nm for the nanoparticles capped with 4-*tert*-butylstyrene, 4-methoxystyrene, and 4-(trifluoromethyl)styrene, respectively, as a result of the decreasing rate of dehydrogenation with the increasing Taft (polar) constant of the *para*-substituents. Importantly, the resulting nanoparticles exhibited unique photoluminescence, where an increase of the Hammett constant of the *para*-substituents corresponded to a blue-shift of the photoluminescence emission, suggesting an enlargement of the HOMO–LUMO band gap of the nanoparticle-bound acetylene moieties. Furthermore, the resulting nanoparticles exhibited apparent electrocatalytic activity towards oxygen reduction in acidic media, with the best performance among the series of samples observed with the 4-*tert*-butylstyrene-capped nanoparticles due to an optimal combination of the nanoparticle core size and ligand effects on the bonding interactions between platinum and oxygen species.

Introduction

Organically functionalized transition metal nanoparticles have been attracting extensive research interests from both fundamental and technological perspectives, as their unique optical and electronic properties can be readily manipulated by the chemical nature of the metal cores, the protecting ligands, and the metal–ligand interfacial bonding interactions.[1–6] In fact, in a series of recent studies, a variety of metal–ligand interfacial bonding interactions have been exploited for nanoparticle surface functionalization.[7–14] Among these, metal–carbene (M=C) π bonds are formed by the self-assembly of diazo derivatives on nanoparticle surfaces,[9–11] whereas metal–acetylide (M–C≡)/–vinylidene (M=C=C) bonds are produced by taking advantage of the strong affinity of acetylene moieties to transition-metal surfaces.[12–23] With the formation of such conjugated bonds at the metal–ligand interface, effective intraparticle charge delocalization occurs between particle-bound functional moieties, as manifested in spectroscopic and electrochemical measurements.[16,19–21] Notably, such nanoparticle-mediated electronic communication has been found to be facilitated by the conducting metal cores and metal–ligand interfacial linkages, which offers a fundamental framework for further and more complicated manipulation of the nanoparticle optical/electronic properties.[11] For instance, for alkyne-caped metal nanoparticles, intraparticle charge delocalization between the particle-bound acetylene moieties may be enhanced (weakened) by the injection (removal) of electrons to (from) the nanoparticle cores, as a result of the manipulation of the metal–ligand bonding interactions.[16] The metal–ligand interfacial bonds may also be readily controlled by deliberate modification of the organic capping ligands with selected functional moieties that exhibit specific interactions with certain molecules and ions.[21,24,25]

More recently, it has been shown that olefin derivatives may also be exploited as a new kind of capping ligand for the preparation of stable Pt nanoparticles.[22] It was found that the resulting nanoparticles exhibited photoluminescence in the visible range, similar to that of Pt nanoparticles functionalized with acetylene derivatives.[15–23] Spectroscopic and electrochemical measurements revealed that the nanoparticles might

Department of Chemistry and Biochemistry, University of California, 1156 High Street, Santa Cruz, California 95064, USA. E-mail: shaowei@ucsc.edu

†Electronic supplementary information (ESI) available: TGA curves and additional voltammograms. See DOI: 10.1039/c6nr02296k

involve the formation of platinum–acetylide (Pt–C≡) or Pt–vinylidene (Pt=C=C) interfacial bonds on the Pt nanoparticle surface, as a result of dehydrogenation and transformation of the olefin moieties catalyzed by the Pt nanoparticles. Mechanistically, the chemical reactivity of the olefin ligands is key to the success of nanoparticle surface functionalization. This is the primary motivation for the present study, where we employ a series of *para*-substituted styrene derivatives as capping ligands for platinum nanoparticle surface functionalization, and examine and compare the chemical reactivity of the ligands, the optical properties and electrocatalytic activities of the eventual nanoparticles within the context of the electron-withdrawing properties of the *para*-substituents.

It is well-known that within a multi-substituted phenyl ring, apparent electronic interactions occur between the substituent moieties, which may be quantified by the Hammett constant (σ).[26–30] For instance, the acidity of benzoic acid increases with the increasing Hammett constant (electron-withdrawing) of the *para*-substituent groups.[26,29,30] In fact, for platinum nanoparticles functionalized with *para*-substituted aliphatic fragments (by using diazonium derivatives as the precursors), we have observed that the electrocatalytic activity towards oxygen reduction reaction (ORR) increases markedly with the increasing Hammett constant of the *para*-substituent groups, which is ascribed to subtle diminishment of the nanoparticle core electron density and hence reduced interactions with oxygen intermediates, as predicted by the so-called volcano plot.[28]

Herein, three styrene derivatives with different *para*-substituent groups, 4-*tert*-butylstyrene (TBS), 4-methoxystyrene (MOS), and 4-(trifluoromethyl)styrene (TFMS), were selected as the protecting ligands for nanoparticle functionalization, where the corresponding Hammett constant of the *para*-substituents varied rather widely, ranging from electron-donating methoxy (σ = −0.27) and *tert*-butyl (σ = −0.20) groups to the electron-withdrawing trifluoromethyl group (σ = +0.54).[27] Experimentally, stable nanoparticles were obtained with all three capping ligands and exhibited clearly defined photoluminescence emissions where the peak positions were found to blue-shift with increasing electron-withdrawing capability of the *para*-substituent groups. Moreover, the nanoparticles exhibited apparent electrocatalytic activity towards ORR in acidic media, and the best performance among the series was observed with the TBS-capped nanoparticles, most probably due to an optimal combination of the nanoparticle core size and electronic properties of the *para*-substitution.

Experimental section

Chemicals

Platinum chloride ($PtCl_2$, 99+%, ACROS), sodium acetate trihydrate ($NaOAc{\cdot}3H_2O$, MC&B), sodium carbonate (Na_2CO_3, 99.5%, ACROS), hydrochloric acid (HCl, 37%, ACROS), 4-*tert*-butylstyrene (TBS, 94%, Alfa Aesar), 4-methoxystyrene (MOS, ≥98%, Sigma-Aldrich), and 4-(trifluoromethyl)styrene (TFMS, 96%, Combi-Blocks Inc.) were all used as received. All solvents were obtained from typical commercial resources at their highest purity and used without further treatment. Water was supplied by a Barnstead Nanopure water system (18.3 MΩ cm).

Synthesis of platinum nanoparticles

Styrene derivative functionalized Pt nanoparticles were prepared by adopting the method developed previously.[19,22] Briefly, 0.1 mmol of $PtCl_2$ was dissolved in 1 mL of concentrated HCl (12.1 M) at 80 °C, and the obtained solution was neutralized with Na_2CO_3 and centrifuged to remove undissolved salts. The supernatant as well as 1 mmol of NaOAc were added into 100 mL of 1,2-propanediol. The mixed solution was heated up to 165 °C under vigorous stirring for 1 h, and the appearance of a dark brown color signified the formation of "bare" platinum colloids. Once the colloid solution was cooled down to 60 °C, 0.3 mmol of a styrene derivative (TBS, MOS, or TFMS) dissolved in 40 mL of toluene was added (corresponding to a three-fold molar excess of the organic ligands to $PtCl_2$), and the mixed solution was stirred at 60 °C overnight. It was found that with the TBS ligands, almost all the nanoparticles were transferred to the toluene phase, whereas only partial transfer was achieved with the other two ligands. The toluene phase was collected with a separatory funnel, dried with rotary evaporation, and rinsed extensively with a copious amount of acetonitrile (for TBS) or isooctane (for MOS and TFMS) to remove excess ligands, affording purified nanoparticles which were denoted as PtTBS, PtMOS, and PtTFMS, respectively.

Characterization

The morphology and size of the nanoparticles were characterized by transmission electron microscopic studies (TEM, Philips CM300, 300 kV). ^{1}H NMR spectroscopic measurements were carried out with a Varian Unity Inova 500 MHz NMR spectrometer. UV-vis absorption studies were performed with a Perkin-Elmer Lambda 35 spectrometer with a resolution of 1 nm using a 1 cm quartz cuvette. Photoluminescence characteristics were examined with a PTI fluorospectrometer. Infrared measurements were carried out with a Perkin-Elmer FTIR spectrometer (Spectrum One, at a resolution of 4 cm^{-1}) where the samples were prepared by casting the particle solutions onto a ZnSe disk. Thermogravimetric analysis (TGA) was performed with a Perkin-Elmer Pyris 1 Thermogravimetric Analyzer under an ultrahigh-purity N_2 (99.999%) flow at a temperature rate of 10 °C min^{-1}, where the organic contents (by weight) were estimated to be 13.7% for PtTBS, 18.7% for PtMOS, and 33.4% for PtTFMS nanoparticles (Fig. S1†). X-ray photoelectron spectra (XPS) were recorded with a PHI5400 instrument equipped with an Al K_α source operated at 350 W and at 10^{-9} Torr. The spectra were referenced to the Si 2p peak of a silicon substrate.

Electrochemistry

Electrochemical studies were carried out with a CHI710 electrochemical workstation using a Pt counter electrode and a Ag/AgCl reference electrode at room temperature. Note that the

Ag/AgCl reference electrode was calibrated against a reversible hydrogen electrode (RHE), and the results in the present study were all referred to RHE. The working electrode was a rotating ring-disk electrode (RRDE, AFE7R9GCAU from Pine Instrument Co.) with a glassy carbon disk (GC, diameter 5.61 mm) and a gold ring. The collection efficiency (N) was determined to be 40% by RRDE measurements in 5 mM $K_4Fe(CN)_6$ + 0.1 M KNO_3.[31] The RRDE electrode was prepared according to a procedure proposed by Gloaguen *et al.*,[32] which has also been adopted in a number of ORR studies.[33–38] In a typical experiment, 500 μg of the platinum nanoparticles obtained above was mixed with 2 mg of XC-72 carbon black (corresponding to a nanoparticle : carbon mass ratio of 1 : 4) in 500 μL toluene along with 5 μL of Nafion 117 solution (5 wt%), and dispersed under sonication. A measured volume (*ca.* 5 μL) of the catalyst ink was then dropcast on the freshly polished GC disk of the RRDE. The solvent was evaporated at room temperature yielding a catalyst loading of *ca.* 5 μg.

Results and discussion

As mentioned above, functionalization of Pt nanoparticles by the styrene derivatives was evidenced by the transfer of the nanoparticles from the alcohol phase to toluene. This was due to the replacement of the original acetate ligands by the hydrophobic styrene derivatives that underwent platinum-catalyzed dehydrogenation to produce acetylene derivatives and self-assembled onto the Pt nanoparticle surface forming platinum–vinylidene (Pt═C═C)/–acetylide (Pt–C≡) interfacial bonds (Scheme 1).[22] Fig. 1 depicts the representative TEM micrographs of the three styrene derivative-functionalized Pt nanoparticles. It can be seen that the nanoparticles were all well separated without apparent aggregation, suggesting sufficient protection of the nanoparticles by the capping ligands, due to the apparent chemical reactivity of the olefin moieties on the Pt nanoparticle surface.[22] Interestingly, whereas the same "bare" platinum colloids (average core diameter 2.8 ± 0.6 nm)[19] were used prior to styrene functionalization, the eventual nanoparticles were markedly smaller and exhibited a clear variation of the core size. From the core histograms (Fig. 1 insets), one can see that the majority of the

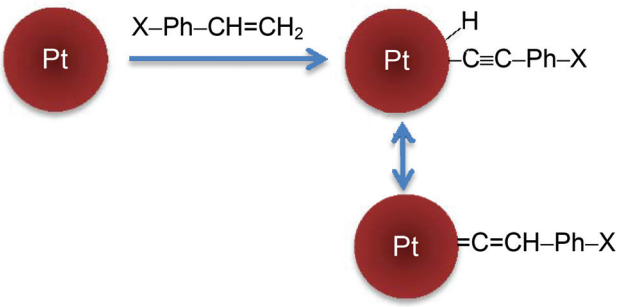

Scheme 1

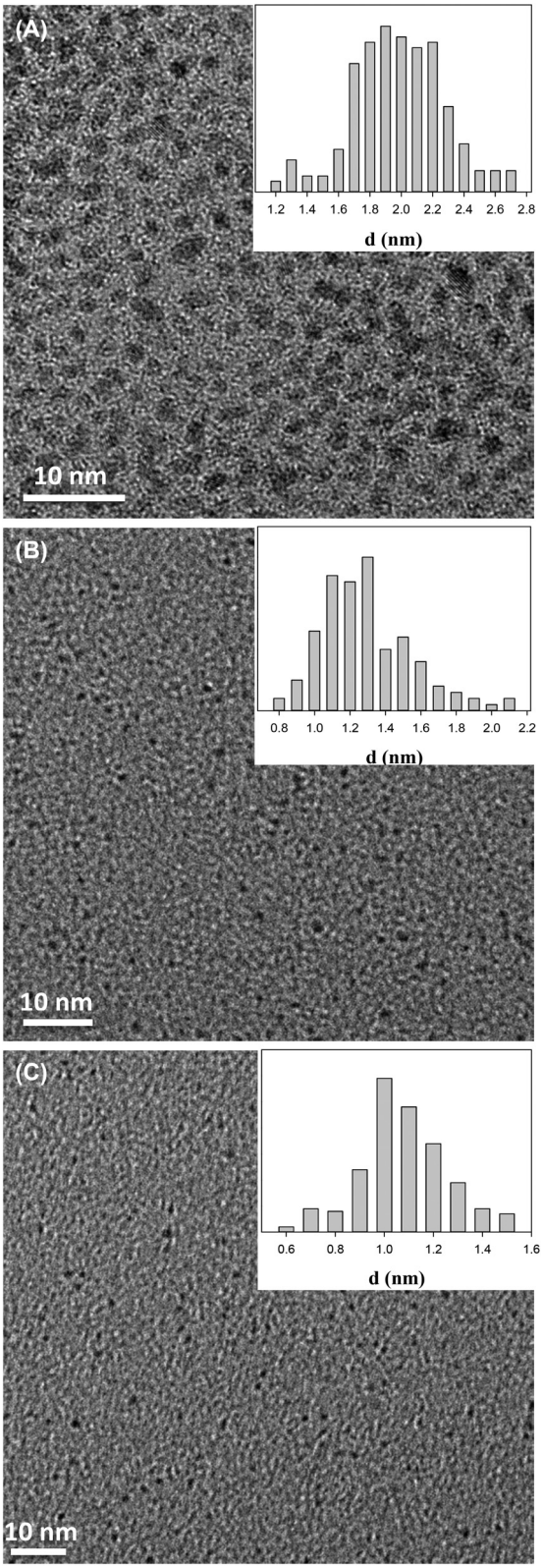

Fig. 1 Representative TEM images of (A) PtTBS, (B) PtMOS, and (C) PtTFMS. Scale bars are all 10 nm. Insets are the corresponding core size histograms.

PtTBS nanoparticles are within the narrow range of 1.7 to 2.3 nm in diameter, with the average diameter at 2.0 ± 0.3 nm. In contrast, the PtMOS nanoparticles were somewhat smaller, mostly between 1.0 and 1.5 nm with the average diameter at 1.3 ± 0.2 nm; and the PtTFMS nanoparticles were even smaller at 1.1 ± 0.2 nm. This suggests a variation of the chemical reactivity of the three styrene derivatives on platinum nanoparticle surfaces. In fact, previous studies have shown that the rate of dehydrogenation reactions depends on the polar effect of the *para*-substituents, decreasing with the increasing Taft (polar) constant (σ^*).[39–41] Of the three styrene derivatives under study, the Taft constant increases in the order of *tert*-butyl (σ^* = −0.30) < methoxy (σ^* = + 1.81) < trifluoromethyl (σ^* = +2.61). That is, in comparison with simple olefin, the rate of dehydrogenation would be enhanced with TBS but diminished with MOS or TFMS. Consequently, dehydrogenation of TBS may occur on Pt nanoparticles of a wide range of particle core sizes whereas for MOS and TFMS they were most likely limited to smaller sizes of the Pt nanoparticles that were more active in catalyzing dehydrogenation reactions.[42–48]

The structures of the obtained Pt nanoparticles were then examined by ^{1}H NMR measurements. Fig. 2 shows the ^{1}H NMR spectra of the PtTBS (black), PtMOS (red), and PtTFMS (green) nanoparticles. For PtTBS nanoparticles the phenyl protons might be identified with the broad peak centered at 7.43 ppm, and the terminal methyl protons at 1.31 ppm. The fact that only broad features were observed suggests that the nanoparticles were spectroscopically clean, and free of excess monomeric ligands[9,11,24,49–51] (the sharp peak at *ca.* 1.60 ppm was due to residual water). This is consistent with the platinum-catalyzed dehydrogenation of the styrene ligands into acetylene derivatives that then self-assembled onto the nanoparticle surface, such that the close proximity to the nanoparticle core surface rendered the signals of relevant protons to be broadened into the baseline.[9,11,24,49–51] Similar behaviors can be found with the other two nanoparticle samples: for PtMOS, the phenyl protons appeared as two broad peaks at 7.33 and 6.96 ppm (due to interactions with the electronegative oxygen moiety), and the methoxy protons at 3.83 ppm, whereas for PtTFMS, the phenyl protons can be identified with the broad peak at 7.69 ppm. It should be noted that the observed variations of the chemical shifts of the phenyl protons are consistent with the electron-withdrawing properties of the *para*-substituents, as manifested by the corresponding Hammett constants (σ): −0.27 for MOS, −0.20 for TBS, and +0.54 for TFMS.[52] Notably, no olefin protons can be found, which are anticipated to emerge at *ca.* 5.22, 5.74, and 6.69 ppm. These observations indicate the successful dehydrogenation of the terminal vinyl groups of the styrene derivatives which were then self-assembled onto the platinum nanoparticle surface and that the nanoparticles were indeed free of excess ligands.

Further structural insights were obtained in FTIR measurements. Fig. 3 depicts the FTIR spectra of the PtTBS (black), PtMOS (red), and PtTFMS (green) nanoparticles. One can see that all three nanoparticles exhibited a small vibrational band at *ca.* 3068 cm^{-1}, which may be assigned to the phenyl ring C–H vibrations. Another rather well-defined vibrational band can be seen at 2039 cm^{-1} for PtTBS, 2057 cm^{-1} for PtMOS, and 2040 and 2084 cm^{-1} for PtTFMS. This may be ascribed to the combined contributions of Pt-hydride (Pt–H)[53,54] and the nanoparticle-bound C≡C stretches that were formed when the olefin moieties were dehydrogenated forming acetylene groups that self-assembled on Pt surfaces[19,22] (Scheme 1). This has been observed previously with alkyne-functionalized transition-metal nanoparticles where intraparticle charge delocalization due to the conjugated metal–ligand interfacial bonds led to a marked red shift of the C≡C vibrational energy, as compared to that of monomeric acetylene moieties.[17,19] Additional vibrational features include the band near

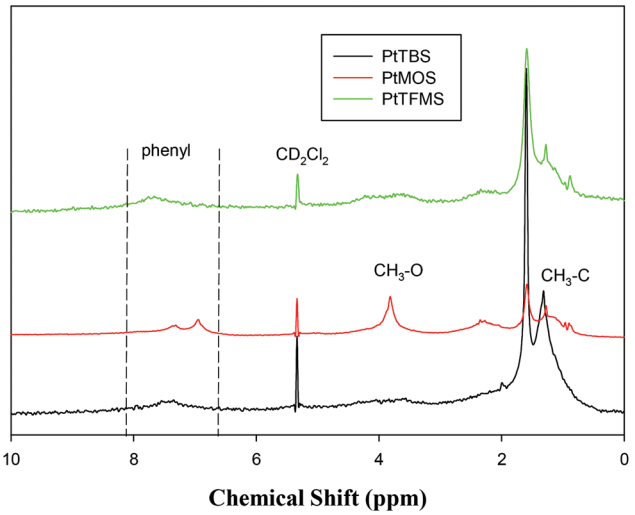

Fig. 2 ^{1}H NMR spectra of PtTBS (black), PtMOS (red), and PtTFMS (green) nanoparticles in CD_2Cl_2.

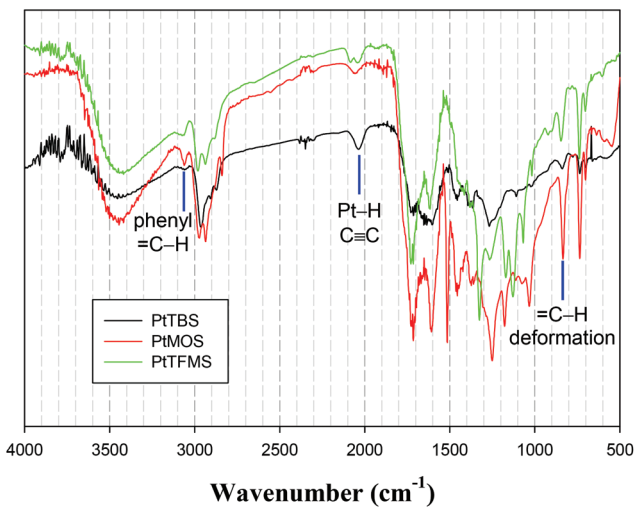

Fig. 3 FTIR spectra of PtTBS (black), PtMOS (red), and PtTFMS (green) nanoparticles.

840 cm^{-1} which most likely arose from the out-of-plane C–H deformation of *para*-substituted phenyl rings. For PtMOS, the C–O–C symmetric stretching can be identified at 1032 cm^{-1}, while the asymmetric stretching bands appear at 1247 cm^{-1} along with two shoulders at 1289 cm^{-1} and 1313 cm^{-1}.[55] For PtTFMS nanoparticles, the C–F asymmetric and symmetric stretching vibrations can be found at 1128 and 1172 cm^{-1}, as well as 1327 cm^{-1} respectively.[56] Furthermore, one may see that no olefin (=C–H) vibrations can be found (>3080 cm^{-1}), signifying that indeed the styrene derivatives underwent dehydrogenation reactions on platinum surfaces forming acetylene moieties that were bound onto the Pt nanoparticles and the resulting nanoparticles were free of monomeric ligands (Fig. 2).

The Pt nanoparticles were then characterized by UV-vis absorption measurements. As depicted in the inset to Fig. 4, the three nanoparticles exhibited only an exponential decay profile with decreasing photon energy, characteristic of nanosized metal particles (the so-called Mie scattering).[57,58] However, the PtMOS (red) and PtTFMS (blue) nanoparticles showed a much steeper decay than PtTBS (black), consistent with the smaller dimensions of the former as determined in TEM measurements (Fig. 1). The photoluminescence characterization was also carried out. As shown in Fig. 4, the PtTBS (black), PtMOS (red), and PtTFMS (blue) nanoparticles all displayed apparent and strong photoluminescence, in contrast to the featureless profile observed with the "bare" platinum colloids (green curves). The observed photoluminescence can be attributed to the formation of Pt–C≡ interfacial bonds as a result of dehydrogenation of the styrene derivatives such that the acetylene moieties bound on the surface of Pt nanoparticles acted analogously to diacetylene derivatives (–C≡C–C≡C–). Similar behaviors have been observed when 1-octadecene was used as the capping ligand.[22] In addition, by using quinine sulphate (1 μM in a 0.05 M H_2SO_4 solution) as a standard, the quantum yields were calculated to be at 0.24%, 5.90%, and 3.90% for the PtTBS, PtMOS, and PtTFMS nanoparticles, respectively.[59,60] A closer analysis shows that the photoluminescence characteristics actually varied rather significantly with the organic capping ligands. Specifically, one can see that the excitation and emission maxima were identified at 380 nm and 455 nm for PtTBS, 385 nm and 475 nm for PtMOS, and 355 nm and 425 nm for PtTFMS. This suggests that the effective HOMO–LUMO band gap of the particle-bound acetylene derivatives decreases in the order of PtTFMS > PtTBS > PtMOS. Notably, it has been demonstrated that a decrease (increase) of the HOMO–LUMO band gap can be induced by the incorporation of electron-donating (-withdrawing) *para*-substituent groups to elevate (lower) the molecular HOMO level.[61–65] In the present study, the Hammett constants (σ) increase in the order of methoxy (−0.27) < *tert*-butyl (−0.20) < trifluoromethyl (+0.54),[26,27] in good agreement with the variation of the observed nanoparticle photoluminescence emissions. The electronic effects from the organic capping ligands were also reflected in the XPS measurements (Fig. S2†), where the binding energies of the Pt 4f electrons increased in the order of PtMOS < PtTBS < PtTFMS, again, consistent with the order of the Hammett constants. One may also note that the nanoparticle core sizes were similar between PtMOS and PtTFMS (Fig. 1), yet these two nanoparticles exhibited markedly different photoluminescence. This suggests that the core size played only a negligible role in determining the nanoparticle photoluminescence; instead, the photoluminescence arose primarily from intraparticle charge delocalization between the nanoparticle-bound acetylene moieties such that they behaved analogously to diacetylene derivatives.[15–23]

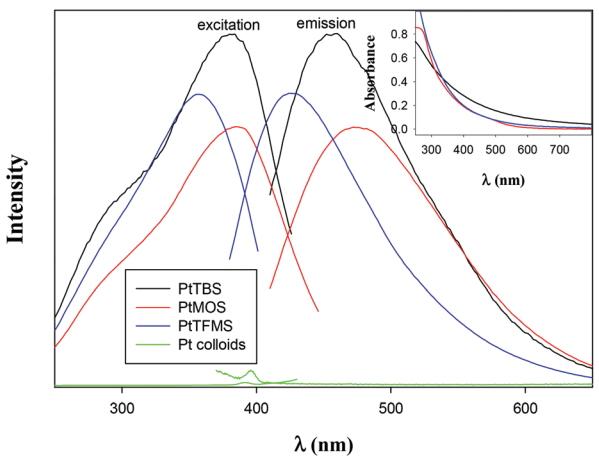

Fig. 4 Excitation and emission spectra of PtTBS (black), PtMOS (red), PtTFMS (blue) nanoparticles in CH_2Cl_2 and "bare" platinum colloids (green) in 1,2-propanediol. Inset shows the corresponding UV-vis absorption spectra of the same nanoparticle solutions in CH_2Cl_2.

The impacts of the *para*-substituent groups on the nanoparticle electrocatalytic activity towards ORR were then examined by voltammetric measurements in acidic media. Prior to ORR tests, the catalyst-modified electrodes were subjected to an electrochemical activation treatment by rapid potential cycling (500 mV s^{-1}) between 0 and +1.2 V (*vs.* RHE) in a nitrogen-saturated 0.1 M $HClO_4$ solution until a steady voltammogram was obtained (Fig. S3†). One can see that both PtTBS and PtTFMS nanoparticles exhibited rather well-defined butterfly voltammetric features, characteristic of platinum electrode surfaces;[28,66–68] yet no such profiles were observed with the PtMOS nanoparticles, implying that it was difficult to electrochemically remove the MOS ligands. This is somewhat unexpected and the origin is not fully understood at this point. One possible explanation is that the strong electron-donating *para*-methoxy groups led to enhanced strength of the metal–ligand interfacial bonds (*vide ante*).[16] Fig. 5(A) depicts the RRDE voltammograms in an oxygen-saturated 0.1 M $HClO_4$ solution at the rotation rate of 1600 rpm. It can be seen that when the electrode potential was swept negatively, nonzero cathodic currents started to emerge for all three samples, suggesting apparent electrocatalytic activity towards ORR; however, the voltammetric profiles clearly differed among the samples. For the PtTBS nanoparticles (black curve), the onset potential for ORR may be identified at around +1.00 V (*vs.* RHE), and the currents reached a plateau at around +0.80 V

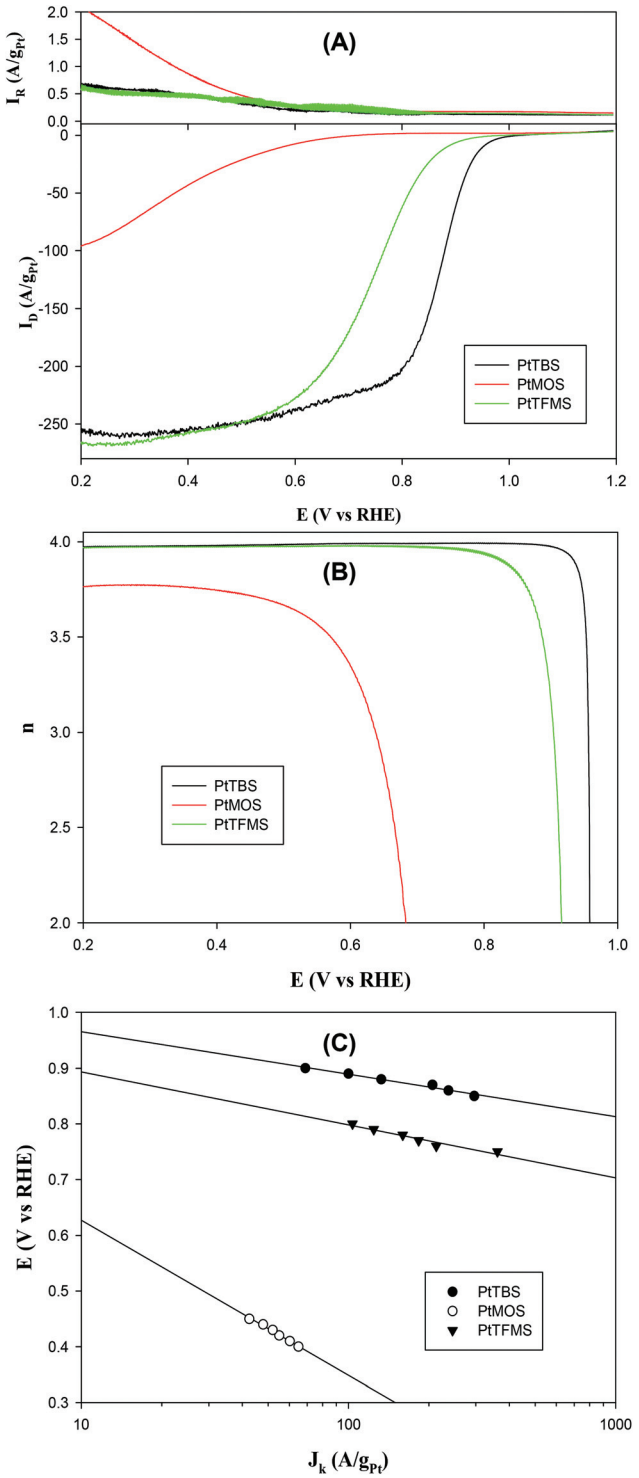

Fig. 5 (A) RRDE voltammograms of a glassy carbon electron modified with PtTBS, PtMOS and PtTFMS nanoparticles in oxygen-saturated 0.1 M $HClO_4$ at the rotation rate of 1600 RPM. Potential sweep rate 10 mV s^{-1}. The nanoparticle loadings were all 5 μg, corresponding to a platinum mass of 4.31, 4.06, and 3.33 μg, respectively, as determined by TGA measurements (Fig. S1†). (B) Variation of the number of electron transfers (n) with electrode potentials. Data were calculated from the RRDE voltammograms in panel (A). (C) Tafel plots of the three nanoparticles. Data were calculated from the RRDE voltammograms in panel (A).

(*vs.* RHE). Such a performance is very comparable to that of commercial Pt/C catalysts.[28] For the PtTFMS nanoparticles, the activity was somewhat lower, where the onset potential was estimated to be +0.95 V and the current plateau was reached at potentials more negative than +0.60 V. However, for the PtMOS nanoparticles, the RRDE voltammograms did not show apparent cathodic currents until the potential was as negative as +0.80 V, and the current plateau was reached at a far more negative potential of around +0.20 V. Furthermore, one may see that the limiting current also varied among the three nanoparticles. For instance, the limiting currents (mass activity) at +0.20 V and 1600 rpm decrease in the order of PtTFMS (258 A g_{Pt}^{-1}) ≈ PtTBS (254 A g_{Pt}^{-1}) ≫ PtMOS (96 A g_{Pt}^{-1}). Taken together, these observations suggest that PtTBS nanoparticles stood out as the best catalyst among the series of styrene-functionalized platinum nanoparticles towards ORR.

In addition, by setting the ring potential at +1.5 V, collection experiments were carried out to monitor the amounts of peroxide intermediates generated during ORR. It can be seen that for all three samples, the ring currents (I_R) were about two orders of magnitude lower than those at the disk (I_D), suggesting that only minimal amounts of peroxide species were generated during oxygen reduction. In fact, the number of electron transfers (n) can be evaluated by the following equation, $n = 4I_D/(I_D + I_R/N)$.[31,69,70] Using the data obtained at 1600 RPM as an example (panel (A)), the n values were calculated for the three samples, as shown in panel (B). It is notable again that the PtTBS nanoparticles exhibited the best ORR performance with the n values above 3.97 within a wide potential range of +0.10 to +0.90 V, suggesting that oxygen primarily underwent four-electron reduction to water, $O_2 + 4H^+ + 4e \rightarrow 2H_2O$, with negligible amounts of peroxide byproducts. PtTFMS nanoparticles also exhibited comparable n values above 3.95 but within a somewhat smaller potential range from +0.10 to +0.80 V. The PtMOS nanoparticles showed the lowest ORR activity among the series, with n values about 3.75 but only at potentials more negative than +0.40 V.

The variation of the electrocatalytic activity towards ORR is further manifested in Koutecky–Levich analysis, where the kinetic current density (I_k) was estimated by removing the diffusion-limited currents (I_L) from the measured voltammetric currents (I_D), $1/I_D = 1/I_L + 1/I_k$. From the Tafel plot in panel (C), one can see that whereas for all three samples the kinetic current density increased markedly with increasingly negative electrode potentials, the activity clearly varied among the samples, decreasing sharply in the order of PtTBS > PtTFMS ≫ PtMOS. Again, the exceedingly low activity of PtMOS might be ascribed to the inaccessibility of the nanoparticle surfaces (Fig. S3†). For the other two nanoparticles, one can see that whereas the *para*-trifluoromethyl group exhibited a higher Hammett constant (σ = +0.54) than the *tert*-butyl group (σ = −0.20), the activity of PtTBS was actually markedly better than that of PtTFMS. At first glance, this seems to contradict the results observed earlier with *para*-substituted aryl-functionalized platinum (Pt–Ar–R, with R = $-CH_3$, –F, –Cl, $-OF_3$, and $-CF_3$) nanoparticles,[28] where the ORR activity was

found to increase with the increasing Hammett constant of the *para*-substituent groups. This was accounted for by the (subtly) weakened interactions of the platinum catalysts with oxygen species, as predicted by the so-called volcano plot. Note that in the prior study,[28] the nanoparticles all fell in the narrow range of core diameters from 1.8 to 2.5 nm. For the PtTBS nanoparticles that are also within this size range (2.0 ± 0.3 nm in diameter, Fig. 1), the ORR activity actually fit nicely in the changing trend of the Pt–Ar–R nanoparticle series.[28] However, for the PtTFMS sample, the nanoparticle core size was substantially smaller at 1.1 ± 0.2 nm (Fig. 1), therefore, although the trifluoromethyl group was more electron-withdrawing, the ORR activity was markedly lower. This suggests that the core size effects played a predominant role in the determination of the nanoparticle ORR activity.[71,72] It might be interpreted by enhanced oxygen adsorption due to the diminished nanoparticle core size,[73,74] as manifested by the more negative peak potential for the electroreduction of platinum oxide, which was +0.67 V for PtTFMS and +0.70 V for PtTBS (Fig. S3†). For PtTBS nanoparticles, the high ORR activity among the series may be ascribed to an optimal combination of the nanoparticle core size and electronic contributions from the *para*-substitutions of the organic ligands.

Conclusions

In this study, stable platinum nanoparticles were prepared by using *para*-substituted styrene derivatives as the capping ligands, as a result of platinum-catalyzed dehydrogenation and transformation of the olefin groups to acetylene moieties that then self-assembled onto the platinum nanoparticle surface forming platinum–vinylidene/–acetylene interfacial bonds. The chemical reactivity of the styrene ligands was found to vary with the Taft (polar) constant of the *para*-substituents, as manifested in TEM measurements where the resulting nanoparticles exhibited a clear variation of the core size. FTIR and NMR spectroscopic measurements confirmed the successful attachments of the organic ligands onto the nanoparticle surface. In photoluminescence measurements a marked discrepancy was observed for the excitation/emission peak positions, suggesting that the HOMO–LUMO band gap of the nanoparticle-bound acetylene moieties might be enlarged by electron-withdrawing *para*-substituents of the capping ligands, and the photoluminescence emission arose largely from intraparticle charge delocalization between the particle-bound acetylene moieties with negligible contributions from the nanoparticle cores. Electrochemically the resulting nanoparticles exhibited apparent electrocatalytic activity towards ORR, with the best performance among the series observed with the PtTBS nanoparticles, due to an optimal combination of the nanoparticle core size and *para*-substitutions of the capping ligands that manipulated the electronic interactions between platinum and oxygen species. These results further highlight the significance of interfacial engineering in the manipulation of nanoparticle optical and electronic properties.

Acknowledgements

This work was supported in part by the National Science Foundation (CHE-1265635 and DMR-1409396). TEM and XPS were carried out at the National Center for Electron Microscopy and Molecular Foundry at the Lawrence Berkeley National Laboratory, respectively, as part of a user project.

References

1 S. W. Chen, in *Electroanalytical Chemistry*, ed. A. J. Bard and C. G. Zoski, 2010, vol. 23, pp. 171–210.
2 R. W. Murray, *Chem. Rev.*, 2008, **108**, 2688–2720.
3 S. W. Chen, Z. H. Zhao and H. Liu, *Annu. Rev. Phys. Chem.*, 2013, **64**, 221–245.
4 G. Yang, L. Hu, T. D. Keiper, P. Xiong and D. T. Hallinan Jr., *Langmuir*, 2016, **32**, 4022–4033.
5 V. A. Vasantha, C. Junhui, T. B. Ying and A. Parthiban, *Langmuir*, 2015, **31**, 11124–11134.
6 B. Wang, J. Li, G. Wang, W. Liang, Y. Zhang, L. Shi, Z. Guo and W. Liu, *ACS Appl. Mater. Interfaces*, 2013, **5**, 1827–1839.
7 F. Mirkhalaf, J. Paprotny and D. J. Schiffrin, *J. Am. Chem. Soc.*, 2006, **128**, 7400–7401.
8 L. Laurentius, S. R. Stoyanov, S. Gusarov, A. Kovalenko, R. Du, G. P. Lopinski and M. T. McDermott, *ACS Nano*, 2011, **5**, 4219–4227.
9 W. Chen, J. R. Davies, D. Ghosh, M. C. Tong, J. P. Konopelski and S. W. Chen, *Chem. Mater.*, 2006, **18**, 5253–5259.
10 X. W. Kang, W. Chen, N. B. Zuckerman, J. P. Konopelski and S. W. Chen, *Langmuir*, 2011, **27**, 12636–12641.
11 W. Chen, S. W. Chen, F. Z. Ding, H. B. Wang, L. E. Brown and J. P. Konopelski, *J. Am. Chem. Soc.*, 2008, **130**, 12156–12162.
12 S. Zhang, K. L. Chandra and C. B. Gorman, *J. Am. Chem. Soc.*, 2007, **129**, 4876–4877.
13 P. Maity, S. Takano, S. Yamazoe, T. Wakabayashi and T. Tsukuda, *J. Am. Chem. Soc.*, 2013, **135**, 9450–9457.
14 M. J. Ford, R. C. Hoft and A. McDonagh, *J. Phys. Chem. B*, 2005, **109**, 20387–20392.
15 W. Chen, N. B. Zuckerman, X. W. Kang, D. Ghosh, J. P. Konopelski and S. W. Chen, *J. Phys. Chem. C*, 2010, **114**, 18146–18152.
16 X. W. Kang, N. B. Zuckerman, J. P. Konopelski and S. W. Chen, *Angew. Chem., Int. Ed.*, 2010, **49**, 9496–9499.
17 X. W. Kang, N. B. Zuckerman, J. P. Konopelski and S. W. Chen, *J. Am. Chem. Soc.*, 2012, **134**, 1412–1415.
18 X. W. Kang and S. W. Chen, *Nanoscale*, 2012, **4**, 4183–4189.
19 K. Liu, X. W. Kang, Z. Y. Zhou, Y. Song, L. J. Lee, D. Tian and S. W. Chen, *J. Electroanal. Chem.*, 2013, **688**, 143–150.

20 B. D. Phebus, Y. Yuan, Y. Song, P. G. Hu, Y. Abdollahian, Q. X. Tong and S. W. Chen, *Phys. Chem. Chem. Phys.*, 2013, **15**, 17647–17653.
21 P. G. Hu, Y. Song, M. D. Rojas-Andrade and S. W. Chen, *Langmuir*, 2014, **30**, 5224–5229.
22 P. G. Hu, P. N. Duchesne, Y. Song, P. Zhang and S. W. Chen, *Langmuir*, 2015, **31**, 522–528.
23 P. G. Hu, Y. Song, L. M. Chen and S. W. Chen, *Nanoscale*, 2015, **7**, 9627–9636.
24 W. Chen, N. B. Zuckerman, J. W. Lewis, J. P. Konopelski and S. W. Chen, *J. Phys. Chem. C*, 2009, **113**, 16988–16995.
25 X. W. Kang, X. Li, W. M. Hewitt, N. B. Zuckerman, J. P. Konopelski and S. W. Chen, *Anal. Chem.*, 2012, **84**, 2025–2030.
26 L. P. Hammett, *J. Am. Chem. Soc.*, 1937, **59**, 96–103.
27 C. Hansch, A. Leo and R. W. Taft, *Chem. Rev.*, 1991, **91**, 165–195.
28 Z. Y. Zhou, X. W. Kang, Y. Song and S. W. Chen, *J. Phys. Chem. C*, 2012, **116**, 10592–10598.
29 C. A. Hollingsworth, P. G. Seybold and C. M. Hadad, *Int. J. Quantum Chem.*, 2002, **90**, 1396–1403.
30 Y. Huang, L. H. Liu, W. H. Liu, S. G. Liu and S. B. Liu, *J. Phys. Chem. A*, 2011, **115**, 14697–14707.
31 Z. Y. Zhou, X. W. Kang, Y. Song and S. W. Chen, *Chem. Commun.*, 2012, **48**, 3391–3393.
32 F. Gloaguen, F. Andolfatto, R. Durand and P. Ozil, *J. Appl. Electrochem.*, 1994, **24**, 863–869.
33 N. M. Markovic, T. J. Schmidt, V. Stamenkovic and P. N. Ross, *Fuel Cells*, 2001, **1**, 105–116.
34 R. Y. Wang, C. X. Xu, X. X. Bi and Y. Ding, *Energy Environ. Sci.*, 2012, **5**, 5281–5286.
35 M. H. Shao, T. Yu, J. H. Odell, M. S. Jin and Y. N. Xia, *Chem. Commun.*, 2011, **47**, 6566–6568.
36 I. Spanos, C. P. Rellan, L. Altmann, M. Baumer and M. Arenz, *Int. J. Hydrogen Energy*, 2014, **39**, 9143–9148.
37 C. Wang, N. M. Markovic and V. R. Stamenkovic, *ACS Catal.*, 2012, **2**, 891–898.
38 Q. W. Tang, L. H. Jiang, J. Liu, S. L. Wang and G. Q. Sun, *ACS Catal.*, 2014, **4**, 457–463.
39 D. Gulkova and M. Kraus, *J. Mol. Catal.*, 1994, **87**, 47–55.
40 M. C. Yang, R. M. Rioux and G. A. Somorjai, *J. Catal.*, 2006, **237**, 255–266.
41 M. T. Buelow and A. J. Gellman, *J. Mol. Catal. A: Chem.*, 1998, **131**, 55–70.
42 R. M. Rioux, B. B. Hsu, M. E. Grass, H. Song and G. A. Somorjai, *Catal. Lett.*, 2008, **126**, 10–19.
43 S. Vajda, M. J. Pellin, J. P. Greeley, C. L. Marshall, L. A. Curtiss, G. A. Ballentine, J. W. Elam, S. Catillon-Mucherie, P. C. Redfern, F. Mehmood and P. Zapol, *Nat. Mater.*, 2009, **8**, 213–216.
44 K. Kon, S. M. A. H. Siddiki and K. I. Shimizu, *J. Catal.*, 2013, **304**, 63–71.
45 J. Zhu, M. L. Yang, Y. D. Yu, Y. A. Zhu, Z. J. Sui, X. G. Zhou, A. Holmen and D. Chen, *ACS Catal.*, 2015, **5**, 6310–6319.
46 M. Nakamura, M. Yamada and A. Amano, *J. Catal.*, 1975, **39**, 125–133.
47 M. S. Kumar, D. Chen, J. C. Walmsley and A. Holmen, *Catal. Commun.*, 2008, **9**, 747–750.
48 M. S. Kumar, D. Chen, A. Holmen and J. C. Walmsley, *Catal. Today*, 2009, **142**, 17–23.
49 W. Chen, N. B. Zuckerman, J. P. Konopelski and S. W. Chen, *Anal. Chem.*, 2010, **82**, 461–465.
50 M. J. Hostetler, J. E. Wingate, C. J. Zhong, J. E. Harris, R. W. Vachet, M. R. Clark, J. D. Londono, S. J. Green, J. J. Stokes, G. D. Wignall, G. L. Glish, M. D. Porter, N. D. Evans and R. W. Murray, *Langmuir*, 1998, **14**, 17–30.
51 R. H. Terrill, T. A. Postlethwaite, C. H. Chen, C. D. Poon, A. Terzis, A. D. Chen, J. E. Hutchison, M. R. Clark, G. Wignall, J. D. Londono, R. Superfine, M. Falvo, C. S. Johnson, E. T. Samulski and R. W. Murray, *J. Am. Chem. Soc.*, 1995, **117**, 12537–12548.
52 R. M. Silverstein, G. C. Bassler and T. C. Morrill, *Spectrometric identification of organic compounds*, Wiley, New York, 5th edn, 1991.
53 H. D. Kaesz and R. B. Saillant, *Chem. Rev.*, 1972, **72**, 231–281.
54 H. C. Clark and W. S. Tsang, *J. Am. Chem. Soc.*, 1967, **89**, 529–533.
55 A. R. Katritzky and N. A. Coats, *J. Chem. Soc.*, 1959, 2062–2066.
56 R. R. Randle and D. H. Whiffen, *J. Chem. Soc.*, 1955, 1311–1313.
57 J. A. Creighton and D. G. Eadon, *J. Chem. Soc., Faraday Trans.*, 1991, **87**, 3881–3891.
58 P. K. Jain, K. S. Lee, I. H. El-Sayed and M. A. El-Sayed, *J. Phys. Chem. B*, 2006, **110**, 7238–7248.
59 A. M. Brouwer, *Pure Appl. Chem.*, 2011, **83**, 2213–2228.
60 K. Suzuki, A. Kobayashi, S. Kaneko, K. Takehira, T. Yoshihara, H. Ishida, Y. Shiina, S. Oishic and S. Tobita, *Phys. Chem. Chem. Phys.*, 2009, **11**, 9850–9860.
61 L. Zophel, V. Enkelmann and K. Mullen, *Org. Lett.*, 2013, **15**, 804–807.
62 G. L. Eakins, J. S. Alford, B. J. Tiegs, B. E. Breyfogle and C. J. Stearman, *J. Phys. Org. Chem.*, 2011, **24**, 1119–1128.
63 P. A. Priya, C. P. Kala and D. J. Thiruvadigal, *Int. J. Nanoelectron. Mater.*, 2010, **3**, 1–7.
64 C. P. Hsieh, H. P. Lu, C. L. Chiu, C. W. Lee, S. H. Chuang, C. L. Mai, W. N. Yen, S. J. Hsu, E. W. G. Diau and C. Y. Yeh, *J. Mater. Chem.*, 2010, **20**, 1127–1134.
65 J. Wu, S. X. Liu, A. Neels, F. Le Derf, M. Salle and S. Decurtins, *Tetrahedron*, 2007, **63**, 11282–11286.
66 G. Q. He, Y. Song, K. Liu, A. Walter, S. Chen and S. W. Chen, *ACS Catal.*, 2013, **3**, 831–838.
67 N. M. Markovic and P. N. Ross, *Electrochim. Acta*, 2000, **45**, 4101–4115.
68 J. S. Spendelow and A. Wieckowski, *Phys. Chem. Chem. Phys.*, 2004, **6**, 5094–5118.
69 W. H. Niu, L. G. Li, X. J. Liu, N. Wang, J. Liu, W. J. Zhou, Z. H. Tang and S. W. Chen, *J. Am. Chem. Soc.*, 2015, **137**, 5555–5562.

70 Y. F. Tang, B. L. Allen, D. R. Kauffman and A. Star, *J. Am. Chem. Soc.*, 2009, **131**, 13200–13201.
71 M. H. Shao, A. Peles and K. Shoemaker, *Nano Lett.*, 2011, **11**, 3714–3719.
72 F. J. Perez-Alonso, D. N. McCarthy, A. Nierhoff, P. Hernandez-Fernandez, C. Strebel, I. E. L. Stephens, J. H. Nielsen and I. Chorkendorff, *Angew. Chem., Int. Ed.*, 2012, **51**, 4641–4643.
73 P. Briot, A. Auroux, D. Jones and M. Primet, *Appl. Catal.*, 1990, **59**, 141–152.
74 B. C. Han, C. R. Miranda and G. Ceder, *Phys. Rev. B: Condens. Matter*, 2008, **77**, 075410.